J Mater Sci **(2022) 57:351–365**

Composites & nanocomposites

Hexacyanoferrate-modified polyvinyl alcohol/graphene oxide aerogel as an efficient and retrievable adsorbent for cesium

Jiang-Bo Huo[1] and Guoce Yu[1,*]

[1] *Laboratory of Environmental Technology, INET, Tsinghua University, Beijing 100084, China*

Received: 3 June 2021
Accepted: 28 September 2021
Published online:
7 October 2021

ABSTRACT

While hexacyanoferrate and its analogues are specific adsorbents for elimination of cesium ions (Cs^+), they seem to encounter a major challenge of separation from solution. To solve this difficulty, a novel aerogel adsorbent (polyvinyl alcohol/graphene oxide/$KNi[Fe(CN)_6]$, denoted as PVA/GO/$KNi[Fe(CN)_6]$) was designed by a synergistic cross-linking reaction coupled with in situ precipitation strategy. PVA and Ni^{2+} firstly played synergistic roles in reinforcement of interwoven structure, and Ni^{2+} coordinated with $[Fe(CN)_6]^{3-}$ to produce $KNi[Fe(CN)_6]$ in situ in the following step. Characterization analysis revealed a hierarchical structure of the aerogel composed of GO sheets and nanoparticles. This unique structure enhanced adsorption performance compared with PVA/GO. Results indicated that pseudo-second-order model ($R^2 = 0.9971$) and intraparticle diffusion model ($R^2 = 1.000$, 0.9959 and 0.8513) fitted the kinetic data well, suggesting that the rate-limiting step was governed by the chemisorption and diffusion mechanism. Isotherm data were better described by the Langmuir model ($R^2 = 0.9970$), indicating monolayer homogeneous adsorption. The structural investigation verified that the substitution of Cs^+ for K^+ (lattice) or for H^+ (carboxyl groups) was the possible adsorption mechanism. The as-prepared adsorbent exhibited satisfactory adsorption capacity of 47.66 mg/g and a merit of easy separation (as a monolith aerogel) and may be taken as a potential candidate for Cs^+ cleanup.

Handling Editor: Andrea de Camargo.

Address correspondence to E-mail: yugc@tsinghua.edu.cn

https://doi.org/10.1007/s10853-021-06573-y

GRAPHICAL ABSTRACT

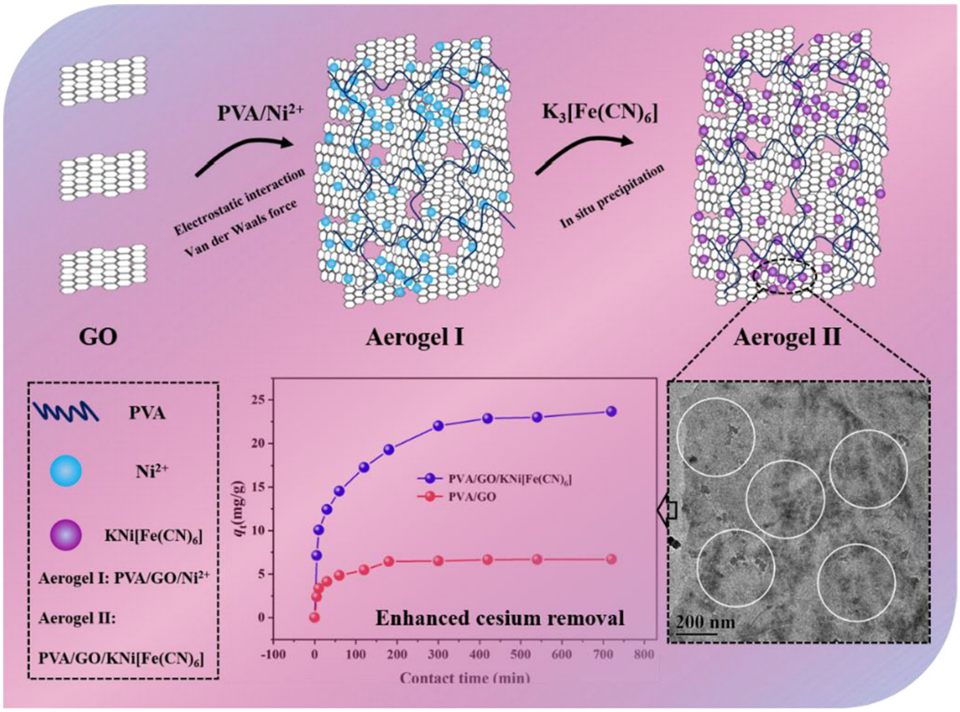

Introduction

There are various nuclides in nuclear wastewater, most of which have a short half-life and low radioactivity [1–3]. However, cesium (Cs) has drawn much attention owing to its strong γ radiation, long half-life (^{37}Cs: 30.17 years, ^{134}Cs: 2.06 years) and easy mobility (as one high-yield (6.09%) fission product of uranium (U^{235})) [3, 4]. Sharing similar property with potassium, sodium and calcium, cesium can easily enter human body and cause severe health issues. Therefore, Cs has been deemed as one of the most hazardous nuclides, and its cleanup is an imperative task in the view of environment protection [5].

Tremendous efforts have been devoted to exploring efficient technologies for removal of cesium [6, 7]. These technologies mainly include solvent evaporation, membrane filtration, electrochemical treatment, adsorption and bioremediation, and adsorption has been considered as one of most promising methods for cesium elimination [8, 9]. To date, various materials have been reported for cesium adsorption, including clays, zeolites, crystalline silicotitanates, layer doubled hydroxides, magnetic adsorbents and Prussian blue-based materials [10].

Prussian blue and its analogues (PB and PBAs), also known as transition metal hexacyanoferrates (HCF), are generally built from transition metal center (Fe, Co, Ni, Cu and Zn) coordinating with cyanide ligand [11–13]. They mainly display a cubic crystal structure and can serve as an ion-sieve in selectively capturing ions with match size (3.2 Å) [14, 15]. Due to high affinity and selectivity for cesium (3.29 Å), this type of materials has been extensively used for removal of cesium [16, 17]. However, pristine PB or PBAs synthesized by precipitation method were ultrafine powder and almost inseparable from water, and this intrinsic drawback severely limited their practical application [18].

To overcome this difficulty, much work has been conducted to develop a variety of porous supports to immobilize PB/PBAs, like biopolymers (chitosan and alginate), porous silicas, magnetic materials and polyvinyl alcohol sponges [18–21]. The immobilization strategy has been demonstrated to be a powerful strategy in addressing the separation problem.

It is well known that there are many oxygen-based functional groups in the graphene oxides, and these groups can contribute to cation adsorption. Presently, graphene and its derivatives as excellent support materials with robust porous network, have received particular attention [22, 23]. Graphene-based nanomaterials display a two-dimensional morphology, and they could be easily assembled into three-dimensional porous aerogel which is significant for separation from solution [22, 24].

The assembly of graphene oxide (GO) can be induced by many methods [25, 26]. For instance, Fe ions have been investigated for fabrication of magnetic GO aerogel [27, 28]. Polyvinyl alcohol (PVA), chitin/chitosan and DNA can also be used as cross-linkers [29–31]. Besides physical methods, chemical reduction is efficient for GO assembly [32]. These resultant GO aerogels possess a large surface area, a structure of abundant pores and low density, and have been intensively investigated as excellent adsorbent-supports [33, 34].

Thus, it is feasible and efficient to integrate good selectivity of PBAs for cesium and easy separability of aerogels from water. The composites mitigating the drawback of PBAs would show promising in practical applications. To the best of our knowledge, there are few studies available on the combination of PBAs and GO aerogels for cesium elimination.

In this study, Ni ions and PVA were chosen as co-cross-linkers for GO self-assembly, and then Ni ions coordinated with $[Fe(CN)_6]^{3-}$ to form precipitate of $KNi[Fe(CN)_6]$ in situ. The resultant material (denoted as PVA/GO/$KNi[Fe(CN)_6]$) displayed a hierarchical structure composed of GO sheets decorated with nanoparticles. Moreover, the adsorption performance of cesium by PVA/GO/$KNi[Fe(CN)_6]$ was investigated including kinetics, isotherms and effects of solution pH and coexisting ions. The immobilization mechanism was also explored by various characterizations.

Experimental section

Materials and reagents

Polyvinyl alcohol (PVA, $M_w \sim 145{,}000$) was supplied by Aladdin Chemical Reagent Co., Ltd. Graphene oxide (GO) dispersion (10 mg/mL) was purchased from Ketan New Materials Co., Ltd. Potassium hexacyanoferrate ($K_3[Fe^{III}(CN)_6]$), nickel sulfate ($NiSO_4 \cdot 6H_2O$), cesium chloride (CsCl), sodium nitrate ($NaNO_3$), potassium nitrate (KNO_3), magnesium nitrate ($Mg(NO_3)_2 \cdot 2H_2O$) and calcium nitrate ($Ca(NO_3)_2 \cdot 6H_2O$) were purchased from Sinopharm Chemical Reagent Co., Ltd. All reagents were of analytical grade, and used directly when received. The non-radioactive standard solution of cesium (1000 mg/L) was purchased from General Research Institute for Nonferrous Metals (Beijing, China). Cesium stock solution was prepared by dissolving CsCl in deionized water.

Synthesis of PVA/GO/$KNi[Fe(CN)_6]$

The detailed synthesis procedures of PVA/GO/$KNi[Fe(CN)_6]$ aerogel were described as follows [35, 36]:

Firstly, 0.2 g of $NiSO_4 \cdot 6H_2O$ and 1.6 g of PVA were dissolved in 100 mL deionized water with vigorous stirring at 80 °C for 2 h. A mixed cross-linker solution was thus obtained. Twenty mL GO dispersion and 5 mL deionized water were blended and kept under ultrasonic treatment for 30 min. Then, 2.5 mL diluted dispersion was transferred to a small vessel. And 0.625 mL of cross-linker solution was dropwise added and stirred rapidly with a fine glass bar. Several seconds later, a hydrogel (PVA/GO/Ni^{2+}) finished cross-linking and was shaped. By freeze-drying (24 h), the hydrogel (PVA/GO/Ni^{2+}) would be transformed into its counterpart aerogel.

Secondly, the aerogel (PVA/GO/Ni^{2+}) was totally immersed into 0.1 mol/L $K_3[Fe(CN)_6]$ solution and kept gently stirring at 50 °C for 6 h, making Ni^{2+} completely converted into $KNi[Fe(CN)_6]$. After that, the as-synthesized hydrogel (PVA/GO/$KNi[Fe(CN)_6]$) was taken out from solution by the aid of tweezers, rinsed repeatedly with deionized water and dried for 24 h in a lyophilizer. Thus, the PVA/GO/$KNi[Fe(CN)_6]$ aerogel was obtained.

Material Characterization

The microstructure and surface elements of as-prepared materials were analyzed on a Hitachi SU-8010 field emission scanning electron microscope (FESEM) equipped with an energy-dispersive X-ray detector (EDX). Transmission electron microscope (TEM) images were observed on a Hitachi-7700 electron microscope. Powder X-ray diffraction (PXRD) patterns were recorded on an X′Pert PRO diffractor with monochromatized Kα radiation (λ = 0.154 nm). Fourier transform infrared spectra (FT-IR) were collected on a Thermo Fisher Scientific Nicolet 6700 instrument. X-ray photoelectron spectroscopy (XPS) was measured on a PHI 5000C ESCA spectrometer with a monochromatized Al *K*α source. The peaks were fitted using XPSPEAK41 software and the binding energy was corrected by a reference (284.5 eV of C 1 s). Nitrogen adsorption–desorption isotherm was performed on a Quantachrome Autosorb-1 chemisorption apparatus at 77 K.

Adsorption experiments

Adsorption experiments were conducted in batch mode. The adsorption kinetics were determined by adding 5 mg adsorbent into 25 mL solution with initial cesium concentration of 4.91 mg/L. At predetermined time intervals, aliquots were withdrawn and filtered. Similarly, the adsorption isotherm experiments were performed within the concentration range of 1.7–21.3 mg/L. Adsorption experiments were allowed for proceeding in a shaker (25 °C) for 12 h to assure adsorption equilibrium.

The effect of solution pH was examined within pH of 3.0–1.0. The interfering ion tests were investigated by separately adding ions (K^+, Na^+, Mg^{2+} and Ca^{2+}) into cesium solution (4.9 mg/L). The mass concentration ratio of interfering ions and cesium ions was approximately 10:1. After adsorption, a small portion of sample solutions were withdrawn and filtered through 0.22 μm syringe filters and analyzed on a polarized Zeeman Atomic Absorption Spectrophotometer (ZA3000 Series AAS, Hitachi, Japan). In this study, adsorption experiments were performed in duplicate and reported by average values. The removal efficiency (*R*, %), adsorption amount (q_t, mg/g) and distribution coefficient (k_d, L/g) were calculated from Eqs. (1), (2) and (3):

$$R = \frac{(C_0 - C_e)}{C_0} \times 100\% \tag{1}$$

$$q_t = \frac{(C_0 - C_t) \times V}{m} \tag{2}$$

$$k_d = \frac{(C_0 - C_e) \times V}{C_e \times m} \tag{3}$$

where C_0, C_t and C_e (mg/L) are the initial concentration, the instant concentration at time t and the equilibrium concentration of cesium ions in the solution, respectively. V (mL) represents the volume of the cesium solution, and m (g) the mass of the adsorbent.

Equations of adsorption kinetics:

Pseudo-first-order model

$$\ln(q_e - q_t) = ln q_e - k_1 t. \tag{4}$$

Pseudo-second-order model

$$\frac{t}{q_t} = \frac{1}{k_2 q_e^2} + \frac{1}{q_e} t. \tag{5}$$

Intraparticle diffusion model

$$q_t = k_i t^{0.5} + C_i \tag{6}$$

where q_t and q_e (mg/g) in Eqs. (1) and (2) represent the instant adsorption amount of cesium ions (t) and the equilibrium adsorption amount of cesium ions (equilibrium time). C_i (mg/g) in Eq. (3) depicts the effect of boundary layer. k_1 (min^{-1}), k_2 [g (mg min)$^{-1}$] and k_i [mg (g min$^{-0.5}$)$^{-1}$] are the rate constants of pseudo-first-order, pseudo-second-order and intraparticle diffusion in Eqs. (4), (5) and (6), respectively.

Equations of adsorption isotherm.

Langmuir model

$$\frac{C_e}{q_e} = \frac{C_e}{q_m} + \frac{1}{K_L q_m}. \tag{7}$$

Freundlich model

$$\ln q_e = \ln K_F + \frac{1}{n} \ln C_e \tag{8}$$

where C_e (mg L^{-1}) and q_e (mg g^{-1}) are the equilibrium concentration of Cs^+ and its corresponding equilibrium adsorption capacity, respectively. K_L (L mg^{-1}) and K_F (mg g^{-1})(L mg^{-1})$^{1/n}$ represent the constant of Langmuir model (Eq. 7) and Freundlich model (Eq. 8), respectively.

Dubinin–Radushkevich (D–R) isotherm (Eq. 9)

$$q_e = q_{\mathrm{maxD}} \exp\left[-\beta\left(\mathrm{RTln}\left(1+\frac{1}{C_e}\right)\right)^2\right] \quad (9)$$

$$E = \frac{1}{(2\beta)^{1/2}} \quad (10)$$

where β ($\mathrm{mol}^2/\mathrm{J}^2$) is a constant related to the mean free energy of adsorption per mole of the adsorbate, q_{maxD} (mmol/g) is the theoretical saturation capacity and ε (J/mol) is the Polanyi potential (= RTln(1 + 1/C_e)), where R (J/mol/K) is the gas constant and T (K) is the absolute temperature. The constant gives an idea about the mean free energy E(J/mol) of adsorption per molecule of the adsorbate when it is transferred to the surface of the solid from infinity in the solution and can be calculated using the relationship in Eq. (10).

Results and discussion

Structure characterization

Figure 1 shows SEM images of PVA/GO and PVA/GO/KNi[Fe(CN)$_6$]. It can be easily observed that an interwoven structure consisted of GO layers and these layers were full of wrinkles as marked in images (Fig. 1a, b). This unique structure may be generated from the strong hydrogen bonds between GO and PVA. After reacting with [Fe(CN)$_6$]$^{3-}$, the interwoven morphology retained and the skeleton seemed to be strengthened. It is interesting that many nanoparticles can be even identified in the wrinkle space (Fig. 1c, d). In TEM images (Fig. 2), a striking structure of layers decorated with particles can be clearly observed. These particles were dispersedly embedded on a GO layer plane (yellow marks in image). By comparison, we can speculate that these particles were probably KNi[Fe(CN)$_6$] species and the resultant aerogel displayed a hierarchical structure.

As depicted in Fig. 3a, there were several diffraction peaks in the PXRD pattern of PVA/GO/KNi[Fe(CN)$_6$]. The broad peak located around 2θ = 8° can be ascribed to the characteristic peak of GO and the shift (comparing with pristine GO) was probably due to an enlarged d-spacing when the layer PVA molecules were intercalated into GO layers. Other diffraction peaks located at 2θ = 17.3°, 24.6°, 35.0° and 39.5° can be well indexed to (200), (220), (400) and (422) spaces of cubic KNi[Fe(CN)$_6$] phase (JCPDS No. 00-051-1897), respectively [37]. This agreed well with the observation of SEM and TEM.

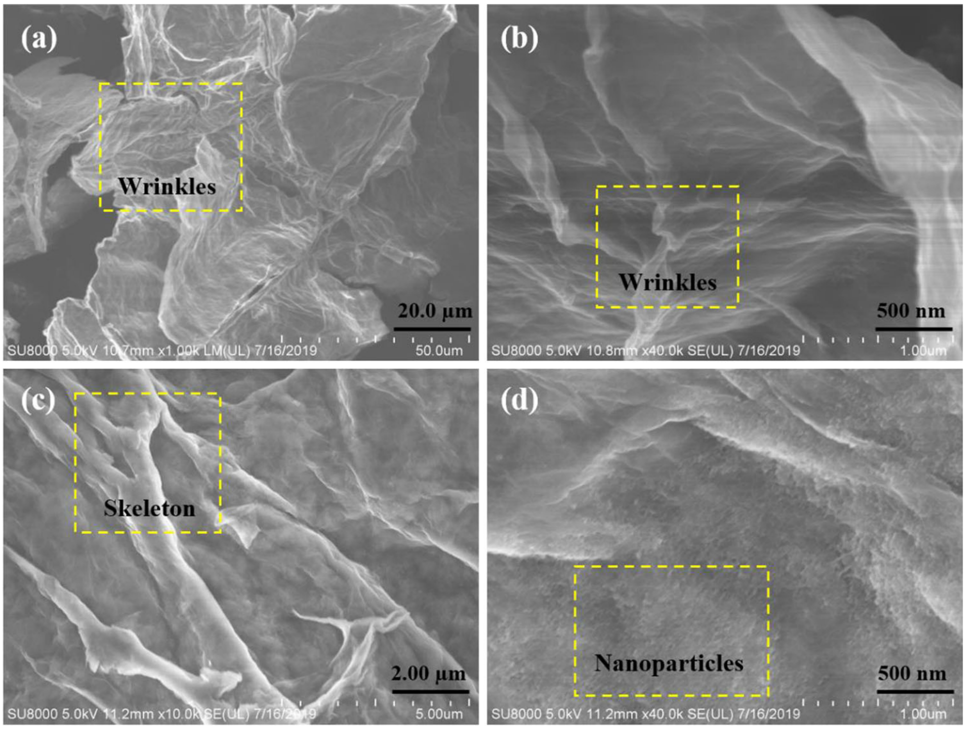

Figure 1 SEM images of PVA/GO (**a**, **b**) and PVA/GO/KNi[Fe(CN)$_6$] (**c**, **d**).

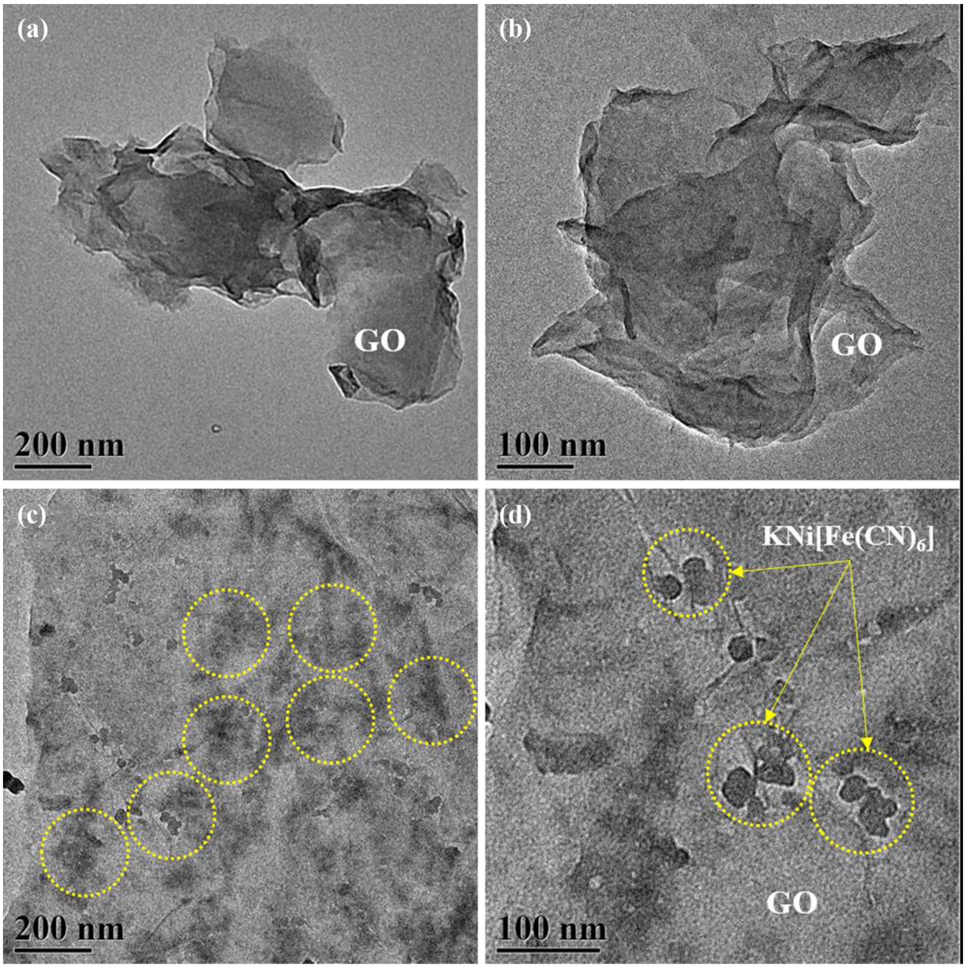

Figure 2 TEM images of GO (**a**, **b**) and PVA/GO/ $KNi[Fe(CN)_6]$ (**c**, **d**).

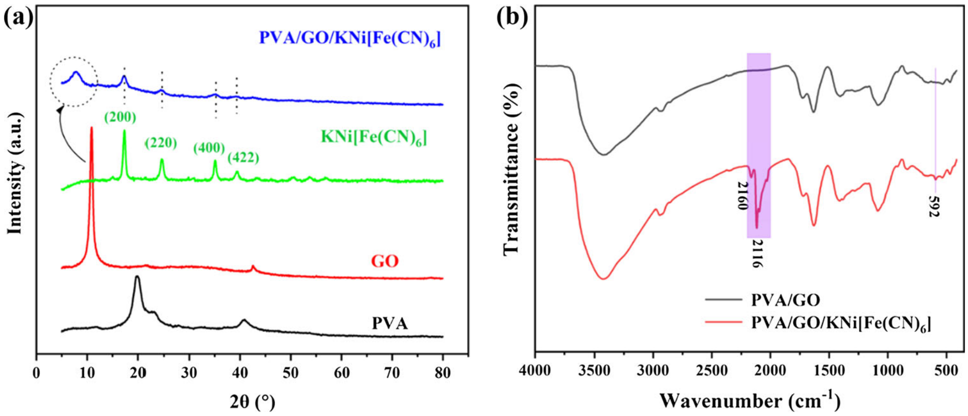

Figure 3 PXRD patterns (**a**) and FT-IR spectra (**b**) of PVA/GO/$KNi[Fe(CN)_6]$.

In comparison to PVA/GO, two typical peaks can be found in FT-IR spectrum of PVA/GO/$KNi[Fe(CN)_6]$ (Fig. 3b). One weak absorption peak around 592 cm^{-1} could be ascribed to the stretching vibration of Fe–N and the other strong absorption peak in the vicinity of 2116 cm^{-1} presented the characteristic vibration of C≡N [18]. These information can confirm the successful formation of $KNi[Fe(CN)_6]$ in the substrate of PVA/GO/Ni^{2+}.

To further obtain insight into the aerogel structure (PVA/GO/$KNi[Fe(CN)_6]$), XPS was used to analyze its surface element composition. As depicted in Fig. 4a, the characteristic peaks of C 1 s, N 1 s, O 1 s, K 2p, Fe 2p and Ni 2p can be identified in XPS

Figure 4 XPS survey of PVA/GO/KNi[Fe(CN)$_6$] (**a**); high-resolution XPS spectra of N 1 s (**b**), Fe 2p (**c**) and Ni 2p (**d**).

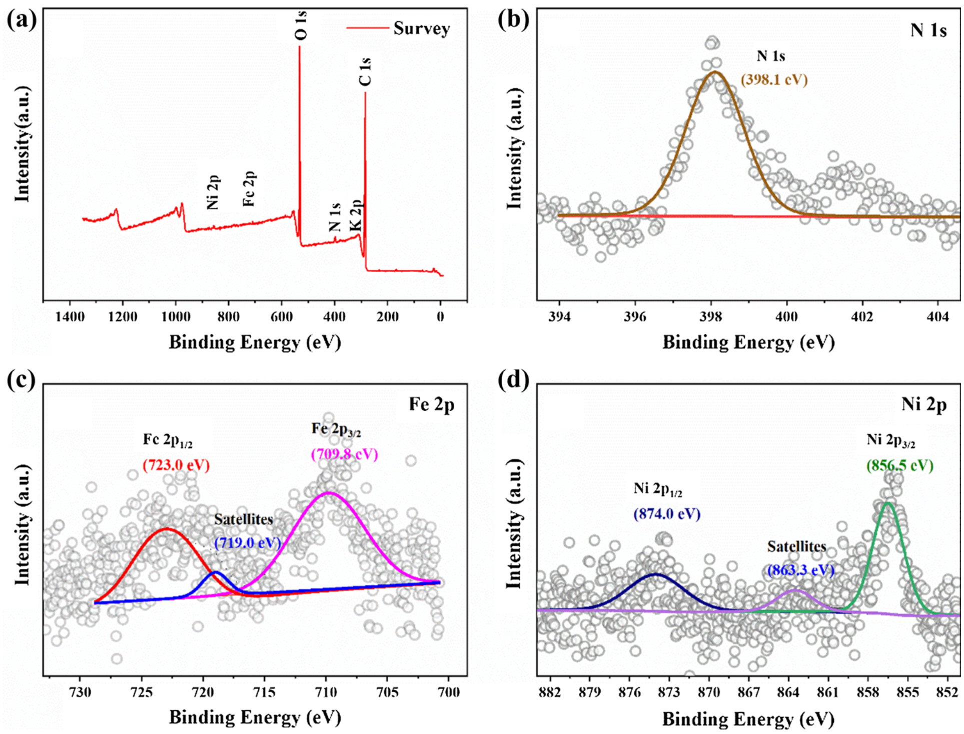

Figure 5 N_2 adsorption–desorption isotherm and pore size distribution of PVA/GO (**a**, **b**) and PVA/GO/KNi[Fe(CN)$_6$] (**c**, **d**).

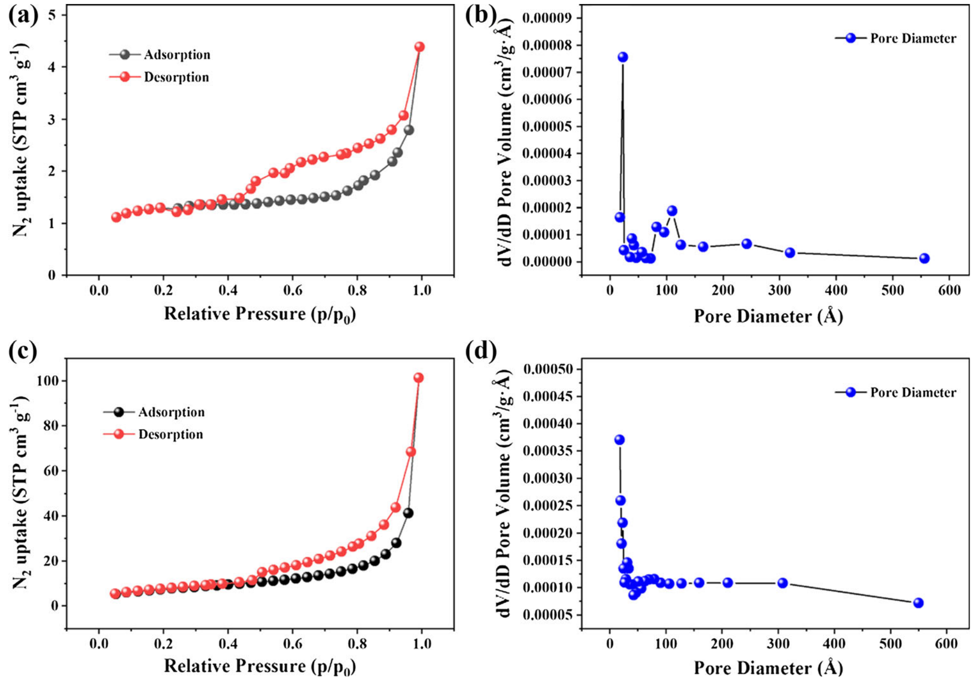

survey. Figure 4b–d shows the high-resolution XPS spectra of N 1 s, Fe 2p and Ni 2p. The peak located in 398.1 eV represented N1s spin orbit. The three peaks in Fe 2p spectra corresponded to Fe 2p3/2 (709.8 eV), Fe 2p1/2 (723.0 eV) and satellite peak (719.0 eV), respectively [38]. The three peaks in Ni 2p spectra corresponded to Ni 2p3/2 (856.5 eV), Ni 2p1/2 (874.0 eV) and satellite peak (7863.3 eV), respectively [39]. The KNi[Fe(CN)$_6$ phase was formed on the PVA/GO surface.

Nitrogen adsorption–desorption isotherm and pore size distribution of PVA/GO and PVA/GO/

KNi[Fe(CN)$_6$] are shown in Fig. 5. The two isotherms both displayed a notable hysteresis loop in the relative pressure of 0.4 to 0.9 and belonged to type IV isotherm, which suggested their mesoporous property (Fig. 5a and c) [40]. The BET specific surface areas (SAA) for PVA/GO and PVA/GO/KNi[Fe(CN)$_6$] were 4.1 and 26.9 m^2/g, while the average pore sizes were 15.9 and 24.8 nm (Fig. 5b and d), respectively. Notably, the phenomenon of increased SAA and pore size was likely associated with the generation of KNi[Fe(CN)$_6$]. Large SAA and broad pore size would be conducive to exposure of active sites and mass transfer of adsorbates [41].

Adsorption performance of PVA/GO/KNi[Fe(CN)$_6$]

The adsorption amount of cesium by PVA/GO and PVA/GO/KNi[Fe(CN)$_6$] increased as the contact time (*t*) increased (Fig. 6a). For both systems, a fast adsorption stage occurred in the first 60 min, and a slow stage followed between 60 and 300 min. Till 720 min, an adsorption equilibrium would occur. While a similar adsorption trend could be shared, the adsorption amount of PVA/GO/KNi[Fe(CN)$_6$] (23.65 mg/g) was as 3.5-fold as that of PVA/GO (6.70 mg/g). The increased adsorption capacity was strongly related to the introduction of KNi[Fe(CN)$_6$] into PVA/GO. For exploring insightful adsorption behavior, three models were used to fit the adsorption data.

Adsorption kinetics

The pseudo-first-order model (PFO), the pseudo-second-order model (PSO) and intraparticle diffusion model (IPD) are shown in Fig. 6b–6d, respectively. The fitting parameters are listed in Table 1. The correlation coefficients (R^2) of PSO (0.9971) and IPD (1.000 and 0.9959 of the first two stages) were higher than that of PFO (0.9744). Moreover, the q_e of PSO (24.41 mg/g) and IPD (20.15 mg/g) was much closer to the experimental value (23.6 mg/g) than that of PFO (13.84 mg/g). It can easily be found that PSO and IPD fitted better for kinetic data than PFO. This demonstrated that the adsorption process was jointly controlled by chemisorption and diffusion mechanism, which may be determined by the unique structure of PVA/GO/KNi[Fe(CN)$_6$] [42].

Adsorption isotherm

The adsorption isotherm was analyzed by the Langmuir model, Freundlich model and Dubinin–Radushkevich model (Fig. 7). The fitting parameters are shown in Table 2. As for isotherm, the adsorption

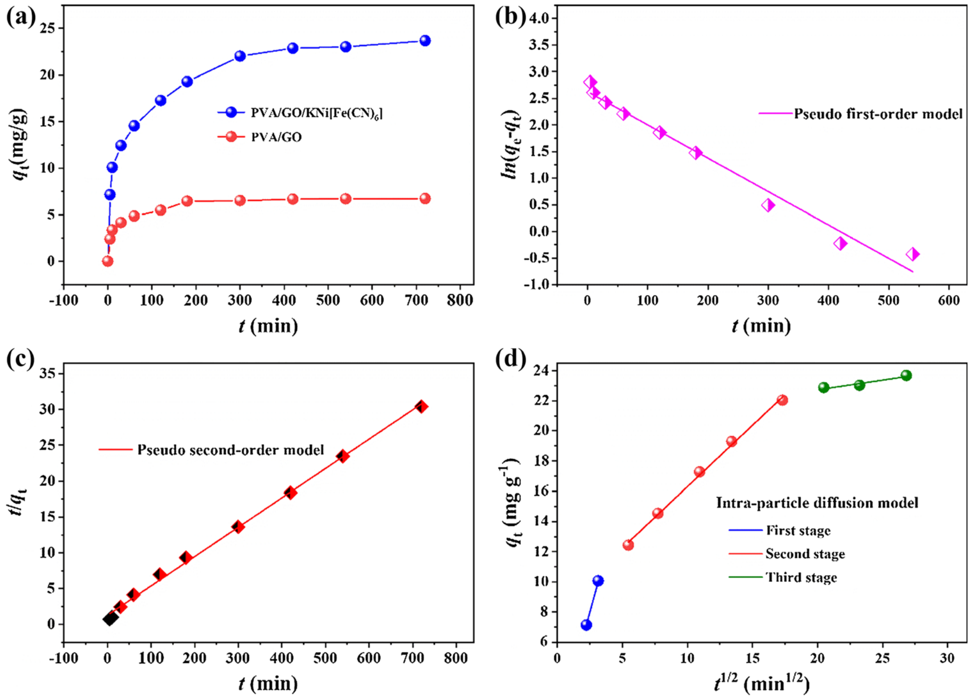

Figure 6 Effect of contact time on adsorption amount of Cs(I) by PVA/GO and PVA/GO/KNi[Fe(CN)$_6$] (**a**); Pseudo-first-order model (**b**); Pseudo-second-order model (**c**) and Intraparticle diffusion model (**d**). Experimental conditions: [Cs(I)]$_0$ = 4.9 mg/L, [adsorbent] = 0.2 g/L, pH = 7.0, T = 298 K.

Table 1 Kinetics parameters of three models (Fig. 6)

Pseudo-first-order model			Pseudo-second-order model			Intraparticle-diffusion model		
$\ln(q_e - q_t) = lnq_e - k_1 t$			$\frac{t}{q_t} = \frac{1}{k_2 \times q_e^2} + \frac{t}{q_e}$			$q_t = k_{id} t^{1/2} + C_i$		
R^2	q_e (mg/g)	k_1 (1/min)	R^2	q_e (mg/g)	k_2 (g/(mg min))	R^2	C_i (mg/g)	k_{id} (mg/g/t$^{1/2}$)
0.9744	13.84	0.00627	0.9971	24.41	0.00132	1.000	0.0604	3.1634
						0.9959	8.1869	0.8120
						0.8513	0.1283	20.156

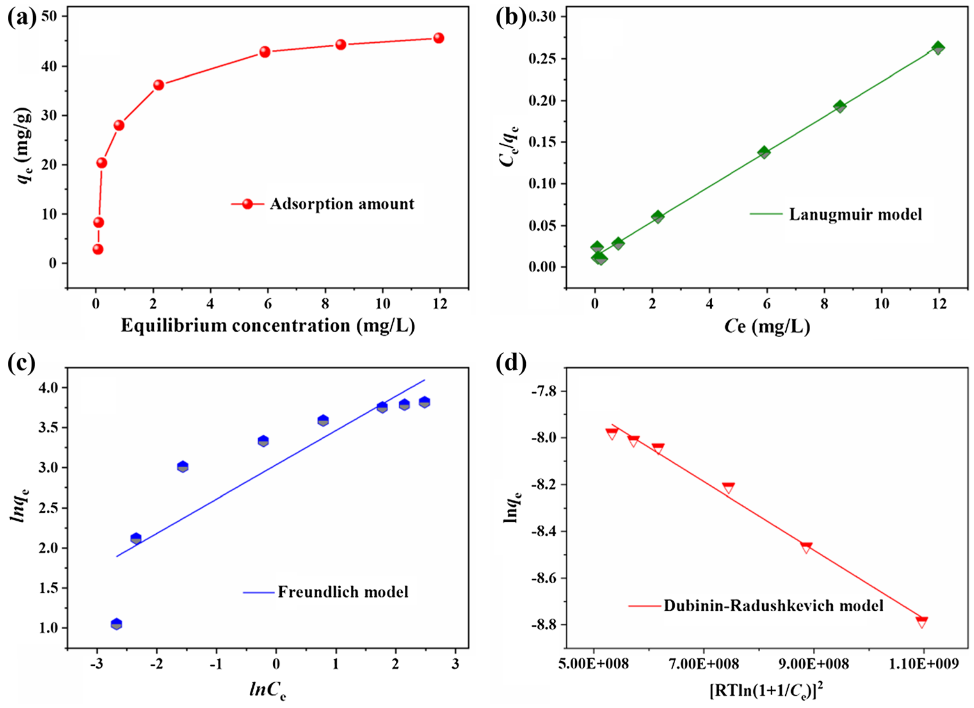

Figure 7 Adsorption isotherm of Cs(I) by PVA/GO/KNi[Fe(CN)$_6$] (**a**), Langmuir model (**b**), Freundlich model (**c**) and Dubinin–Radushkevich model (**d**). Experimental conditions: [Cs(I)]$_0$ = 1.7–21.3 mg/L, [adsorbent] = 0.2 g/L, pH = 7.0, t = 12 h, T = 298 K.

Table 2 Isotherm parameters of three models (Fig. 7)

Langmuir model			Freundlich model			Dubinin–Radushkevich		
$\frac{C_e}{q_e} = \frac{1}{K_L \bullet q_m} + \frac{C_e}{q_e}$			$lnq_e = lnK_F + 1/n \cdot lnC_e$			$lnq_e = lnq_m - \beta\varepsilon^2$ $\varepsilon = RTln(1 + 1/C_e)$		
R^2	q_m (mg/g)	K_L (L/mg)	R^2	n	K_F (mg g^{-1})(L mg^{-1})$^{1/n}$	R^2	q_m (mg/g)	β
0.9970	47.66	1.61	0.7554	2.34	20.88	0.9897	103.1	1.464

amount gradually increased when the initial concentration increased. When the active sites were completely occupied by cesium ions, a saturation adsorption amount can be achieved (Fig. 7a). According to the R^2 (0.9970), it can be understood that the Langmuir model can fit best for adsorption data, indicating this adsorption was mostly a monolayer homogeneous adsorption [43]. The unsatisfactory R^2 suggested the adsorption did not conform to the Freundlich model (R^2 = 0.7554). Calculated from the Langmuir model, the theoretically maximum adsorption capacity (q_m) was 47.66 mg/g. A comparison was made among the cesium adsorbents, listed in Table 3. There are three categories of adsorbents, i.e., chitosan-based hybrids, magnetic composites and Prussian blue-based adsorbents

Table 3 Comparison of Cs(I) adsorption capacity for newly reported adsorbents

Adsorbent	Concentration (mg/L)	Maximum capacity (mg/g)	Ref.
Magnetic bentonite–chitosan	50–500	57.10	[5]
Copper ferrocyanide-embedded magnetic hydrogel	10–500	17.36	[18]
Chitosan/molecular sieve-4A	1–25	44.21	[44]
PVA/PAA/Prussian blue	0.5–20	4.082	[45]
Prussian blue-laden magnetic adsorbents	20–50	58.73	[46]
Montmorillonite–Prussian blue hybrid	20–250	57.47	[47]
PVA/graphene oxide/KNi[Fe(CN)$_6$]	1.7–21.3	47.67	This study

[5, 18, 44–47]. Their adsorption capacity toward cesium ions was among 4.08–58.73 mg/g. The as-prepared aerogel (PVA/GO/KNi[Fe(CN)$_6$]) displayed a comparable adsorption capacity (47.67 mg/g) to most of the adsorbents listed. Considering simple preparation and convenient separation, PVA/GO/KNi[Fe(CN)$_6$ may be a potential adsorbent for cesium.

The Dubinin–Radushkevich model can be used to differentiate the physical adsorption and chemisorption. According to $E = (2\beta)^{-1/2}$, the value of E is 18.5 kJ/mol. Generally, when $E < 8$ kJ/mol, the adsorption behavior belongs to physical sorption; when $E > 8$ kJ/mol, the adsorption behavior belongs to chemisorption [48]. Obviously, the adsorption behavior of cesium by PVA/GO/KNi[Fe(CN)$_6$ was a chemisorption process, and this agreed well with the result of adsorption kinetics.

Effect of solution pH and coexisting ions

The effect of solution initial pH is shown in Fig. 8a. When pH ranged from 5.0 to 9.0, *R* (removal efficiency, %) kept 95.5%. When pH dropped to 3.0 or increased to 11.0, *R* underwent a moderate decline to 81.2% or 74.5%, respectively. In a weak acid system, the decline of *R* may be resulted from protons' competitive influence. However, in an alkaline system, the reason was probably due to the reduction of active sites. As previously reported, a plenty of OH$^-$ may induce a fraction of degradation of KNi[Fe(CN)$_6$.

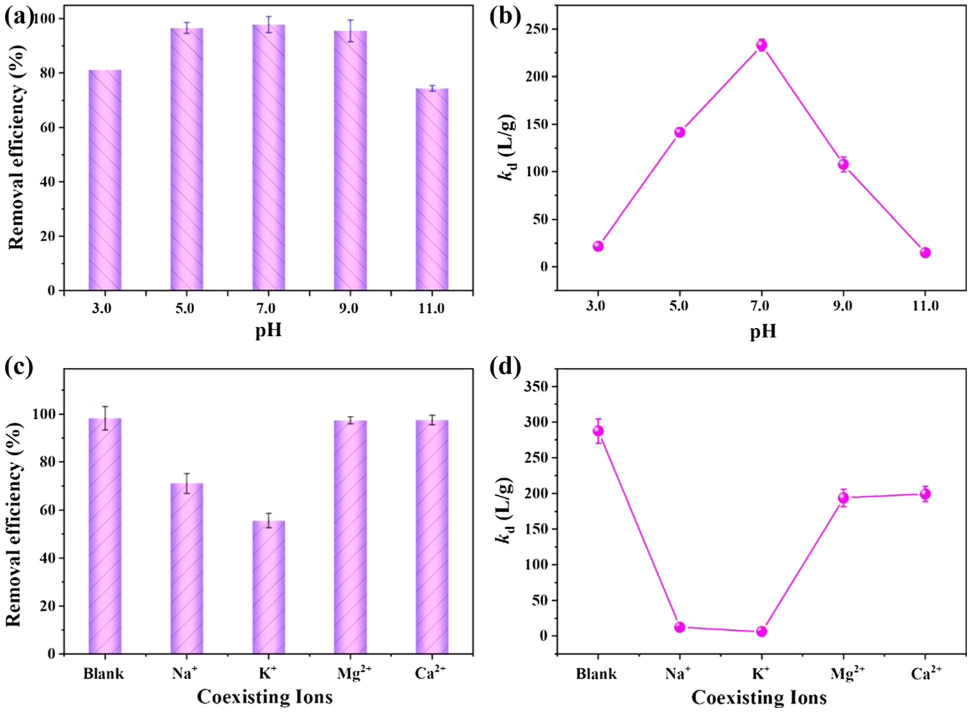

Figure 8 Effect of solution pH (**a**) and the corresponding distribution coefficient (k_d) (**b**); effect of coexisting ions (**c**) and the corresponding distribution coefficient (k_d) (**d**). Experimental conditions: $[Cs(I)]_0$ = 4.9 mg/L, [adsorbent] = 0.2 g/L, pH = 7.0, t = 12 h, T = 298 K.

In a word, PVA/GO/KNi[Fe(CN)$_6$ exhibited excellent removal performance toward cesium ions in neutral solution and was not favored in an acidic or alkaline environment. Evidence can also be found in Fig. 8b. The distribution coefficient (k_d) suffered from a dramatic drop when the solution pH was 3.0 (k_{d-} = 21.5 L/g) or 11.0 (k_d = 15.0 L/g), whereas kd kept above 107.6 L/g when the solution pH was 5.0 to 9.0. These results suggested an acidic or alkaline condition was not conducive to the adsorption [49].

Likewise, the effect of coexisting ions was also investigated (Fig. 8c). In a mixed system, K^+ and Na^+ imposed a severe impact on the *R* of cesium ions, leading to R down to 71.1% and 55.6% from 98.3% (control test), respectively. In contrast, Mg^{2+} and Ca^{2+} showed a very slight effect, and *R* still retained 97.4% and 97.5%, respectively. A similar phenomenon can be found in Fig. 8d. K^+ and Na^+ interfered strongly with the adsorption of cesium ions, making k_d fall down to 12.3 and 6.3 L/g from 287.4 L/g. Mg^{2+} and Ca^{2+} competed slightly with cesium ions, and k_d was 193.7 and 199.3 L/g. As known, K^+ and Na^+ are located in the same group with the cesium ion, and they shared many similar physicochemical properties. In particular, the hydrated radius of K^+ (3.3 Å) and Na^+ (3.6 Å) is much closer to Cs^+ (3.29 Å) [50]. In an ion-exchange process, K^+ and Na^+ would tend to consume many active sites, thus decreasing the adsorption of cesium ions [5].

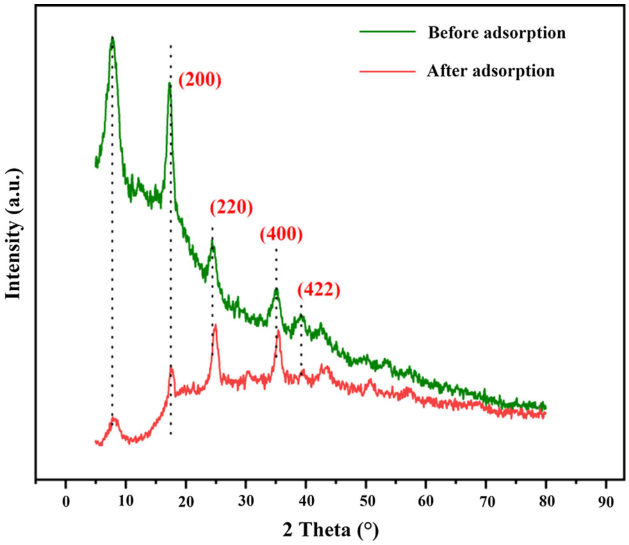

Figure 9 PXRD patterns of PVA/GO/KNi[Fe(CN)$_6$] before and after adsorption of Cs(I).

Adsorption mechanism

To explore the adsorption mechanism, the PXRD patterns of PVA/GO/KNi[Fe(CN)$_6$ before and after adsorption were performed (Fig. 9). After adsorption of cesium, the intensity of characteristic peaks became much weaker, and the positions of peaks displayed a slight shift to the positive direction. This suggested that a replacement of K^+ by Cs^+ may induce a shrinkage of KNi[Fe(CN)$_6$ lattice. In other words, ion-exchange was one of the adsorption mechanisms. Moreover, the SEM–EDX spectra can provide another evidence (Fig. 10). Before adsorption, there was approximately 1.4*wt%* potassium on the surface of the aerogel. After adsorption, there was no signal of potassium on the surface, whereas 3.8*wt%* cesium was obviously detected. This further confirmed the ion-exchange mechanism, as previously reported [47]. In addition, the unique cubic lattice of PB or PBAs may trap a fraction of Cs^+ ions to some extent.

XPS spectra were used to identify adsorption sites and interfacial interaction. As shown in Fig. 11a and b, the peak of Cs 3d can be found in XPS survey spectra and high-resolution spectra. This observation agreed with the results of EDX spectra, strongly suggesting the adsorption of cesium on the surface of the as-prepared aerogel. The peak of K 2p was also analyzed before (Fig. 11c) and after adsorption (Fig. 11d). The characteristic peak of K 2p disappeared after adsorption of cesium, and this indicated the involvement of K^+ in the adsorption process. Moreover, the peak of O 1 s was also measured to investigate the contribution of oxygen-containing functional groups to the adsorption. O 1 s can be deconvoluted into two types of oxygen species (C–O–C/C–O=C and C–OH). The relative content of C–O–C/C–O=C species was 19.83% and 16.22%, while that of C–OH species was 80.47% and 83.78% before and after adsorption. There was a slight shift to high binding energy for C–O–C/C–O=C from 533.48 eV to 534.20 eV, and for C–OH from 532.30 eV to 532.66 eV, respectively. The variation of relative content and binding energy of oxygen species suggested oxygen-containing functional groups may participate in the adsorption process by the way of replacement of protons [46, 51].

Based on the above analysis, the adsorption mechanism of cesium ions by PVA/GO/KNi[Fe(CN)$_6$ was tentatively proposed as shown in

Figure 10 SEM–EDX of PVA/GO/KNi[Fe(CN)$_6$] before (**a**) and after adsorption of Cs(I) (**b**).

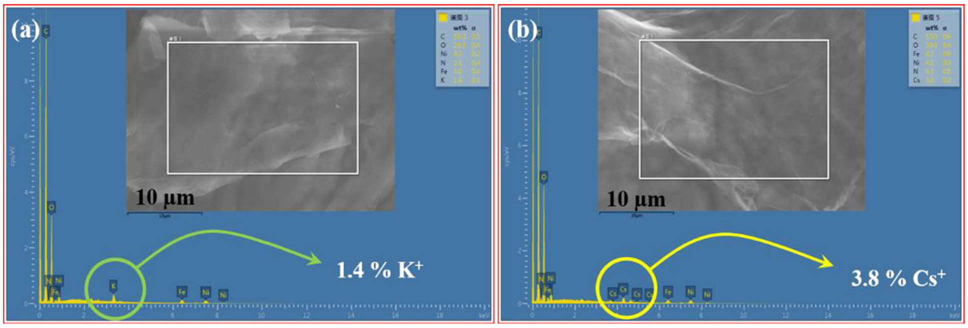

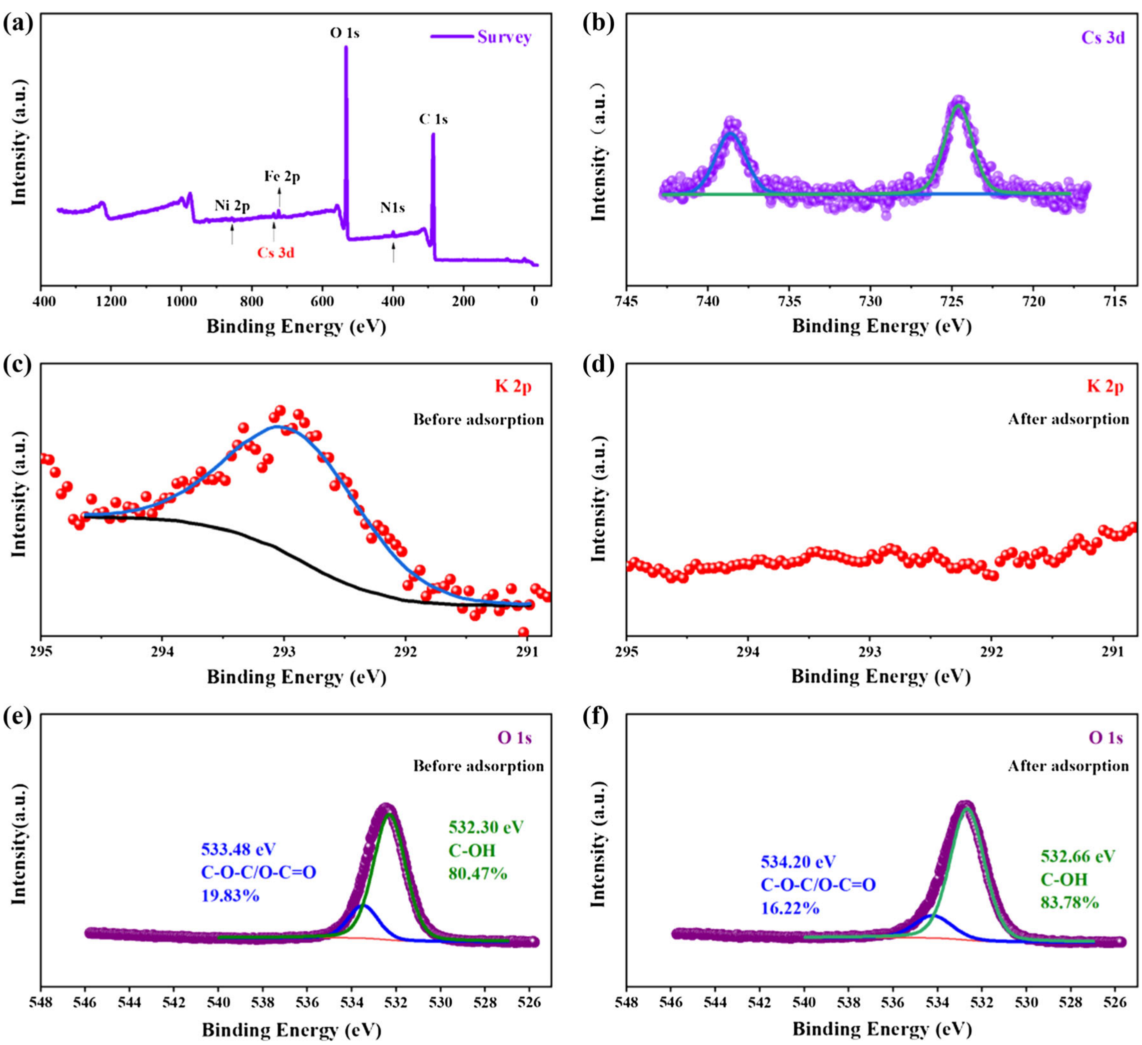

Figure 11 XPS survey of PVA/GO/KNi[Fe(CN)$_6$] after adsorption of Cs(I) (**a**); high-resolution XPS spectra of Cs 3d (**b**); K 2p before adsorption (**c**) and K 2p after adsorption (**d**); O 1 s before adsorption (**e**) and O 1 s after adsorption (**f**).

Fig. 12. There were three immobilization mechanisms involved in the cesium adsorption: (i) the capture of Cs^+ by cubic lattice, (ii) the ion-exchange of K^+ by Cs^+ and (iii) the interaction between electrons of oxygen and cesium orbits (proton substitution) [52, 53].

Conclusions

In summary, a novel aerogel (PVA/GO/KNi[Fe(CN)$_6$]) was successfully fabricated by combining a synergistic cross-linking reaction with in situ precipitation strategy. Ni^{2+} and PVA synergistically

Figure 12 Schematic illustration of adsorption mechanism of Cs(I) by PVA/GO/KNi[Fe(CN)$_6$].

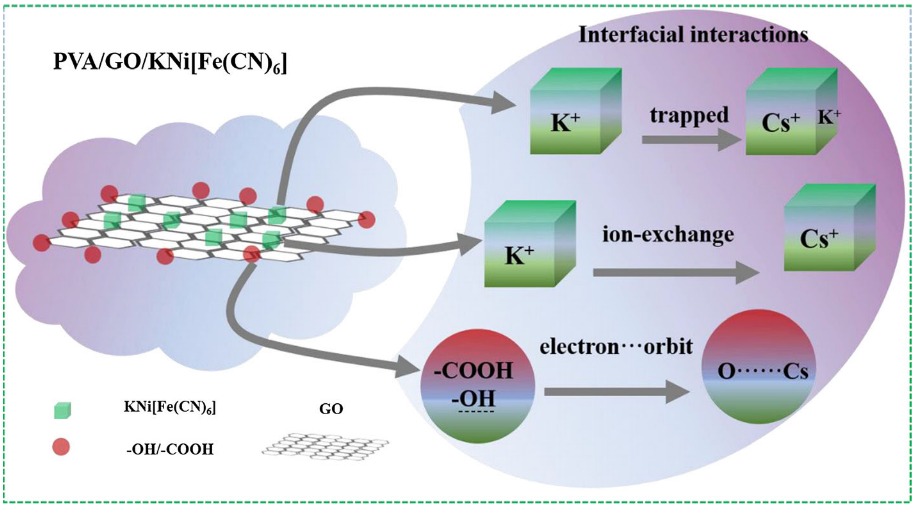

played roles in the assembly of GO units, and then Ni^{2+} in situ coordinated with [Fe(CN)$_6$]$^{3-}$ to produce KNi[Fe(CN)$_6$] in the following stage. The resultant aerogel exhibited a hierarchical structure composed of GO sheets decorated with nanoparticles. Evaluation of adsorption performance indicated pseudo-second-order model and intraparticle diffusion model can better fit the kinetic data, and the Langmuir model can depict the isotherm data appropriately. This indicated the adsorption of Cs$^+$ by the as-prepared aerogel was probably a chemisorption process. Characterization analysis further confirmed that the substitution of Cs$^+$ for K$^+$ (KNi[Fe(CN)$_6$]), the physical capture of Cs$^+$ by the cubic lattice (KNi[Fe(CN)$_6$]) and the proton exchange (carboxyl/hydroxyl) were the possible adsorption mechanism. This aerogel adsorbent showed good adsorption performance (with a capacity of 47.66 mg/g) as well as a merit of easy separation from solution and may be a promising alternative for cesium cleanup.

Funding

This work was supported by a research program from the State Administration of Science, Technology and Industry for National Defence, China ([2017]1474).

References

[1] Liu X, Chen GR, Lee DJ et al (2014) Adsorption removal of cesium from drinking waters: a mini review on use of biosorbents and other adsorbents. Bioresour Technol 160:142–149. https://doi.org/10.1016/j.biortech.2014.01.012

[2] Steinhauser G, Brandl A, Johnson TE (2014) Comparison of the Chernobyl and Fukushima nuclear accidents: a review of the environmental impacts. Sci Total Environ 470:800–817. https://doi.org/10.1016/j.scitotenv.2013.10.029

[3] Husnain SM, Um W, Woojin-Lee W-L, Chang Y-S (2018) Magnetite-based adsorbents for sequestration of radionuclides: a review. RSC Adv 8:2521–2540. https://doi.org/10.1039/c7ra12299c

[4] Zhang H, Hodges CS, Mishra PK et al (2020) Bio-inspired preparation of clay-hexacyanoferrate composite hydrogels as super adsorbents for Cs+. ACS Appl Mater Interfaces 12:33173–33185. https://doi.org/10.1021/acsami.0c06598

[5] Wang K, Ma H, Pu S et al (2019) Hybrid porous magnetic bentonite-chitosan beads for selective removal of radioactive cesium in water. J Hazard Mater 362:160–169. https://doi.org/10.1016/j.jhazmat.2018.08.067

[6] Zhang X, Gu P, Liu Y (2019) Decontamination of radioactive wastewater: state of the art and challenges forward. Chemosphere 215:543–553. https://doi.org/10.1016/j.chemosphere.2018.10.029

[7] Wang J, Zhuang S (2019) Removal of cesium ions from aqueous solutions using various separation technologies. Rev Environ Sci Bio/Technol 18:231–269. https://doi.org/10.1007/s11157-019-09499-9

[8] Feng M, Zhang P, Zhou HC, Sharma VK (2018) Water-stable metal-organic frameworks for aqueous removal of heavy metals and radionuclides: a review. Chemosphere 209:783–800. https://doi.org/10.1016/j.chemosphere.2018.06.114

[9] Wang J, Zhuang S (2020) Cesium separation from radioactive waste by extraction and adsorption based on crown

ethers and calixarenes Nucl. Eng Technol 52(328):336. https://doi.org/10.1016/j.net.2019.08.001

[10] Alby D, Charnay C, Heran M, Prelot B, Zajac J (2018) Recent developments in nanostructured inorganic materials for sorption of cesium and strontium: Synthesis and shaping, sorption capacity, mechanisms, and selectivity-a review. J Hazard Mater 344:511–530. https://doi.org/10.1016/j.jhazmat.2017.10.047

[11] Chen L, Wang X, Zhang X, Zhang H (2012) 3D porous and redox-active prussian blue-in-graphene aerogels for highly efficient electrochemical detection of H_2O_2. J Mater Chem 22:22090. https://doi.org/10.1039/c2jm34541b

[12] Zakaria MB, Chikyow T (2017) Recent advances in Prussian blue and Prussian blue analogues: synthesis and thermal treatments. Coord Chem Rev 352:328–345. https://doi.org/10.1016/j.ccr.2017.09.014

[13] Wang X, Cheng L (2020) Multifunctional Prussian blue-based nanomaterials: preparation, modification, and theranostic applications. Coord Chem Rev 419:213393. https://doi.org/10.1016/j.ccr.2020.213393

[14] Nai J, Lou XWD (2019) hollow structures based on prussian blue and its analogs for electrochemical energy storage and conversion. Adv Mater 31:1706825. https://doi.org/10.1002/adma.201706825

[15] Newton GN, Nihei M, Oshio H (2011) Cyanide-bridged molecular squares—the building units of prussian blue. Eur J Inorg Chem 2011:3031–3042. https://doi.org/10.1002/ejic.201100407

[16] Wang J, Zhuang S, Liu Y (2018) Metal hexacyanoferrates-based adsorbents for cesium removal. Coord Chem Rev 374:430–438. https://doi.org/10.1016/j.ccr.2018.07.014

[17] Olatunji MA, Khandaker MU, Mahmud HNME, Amin YM (2015) Influence of adsorption parameters on cesium uptake from aqueous solutions—a brief review. RSC Adv 5:71658–71683. https://doi.org/10.1039/c5ra10598f

[18] Lee I, Park CW, Yoon SS, Yang HM (2019) Facile synthesis of copper ferrocyanide-embedded magnetic hydrogel beads for the enhanced removal of cesium from water. Chemosphere 224:776–785. https://doi.org/10.1016/j.chemosphere.2019.02.199

[19] Shan S, Tang H, Zhao Y, Wang W, Cui F (2019) Highly porous zirconium-crosslinked graphene oxide/alginate aerogel beads for enhanced phosphate removal. Chem Eng J 359:779–789. https://doi.org/10.1016/j.cej.2018.10.033

[20] Vincent T, Vincent C, Barré Y, Guari Y, Le Saout G, Guibal E (2014) Immobilization of metal hexacyanoferrates in chitin beads for cesium sorption: synthesis and characterization. J Mater Chem A 2:10007. https://doi.org/10.1039/c4ta01128g

[21] Sangvanich T, Sukwarotwat V, Wiacek RJ et al (2010) Selective capture of cesium and thallium from natural waters and simulated wastes with copper ferrocyanide functionalized mesoporous silica. J Hazard Mater 182:225–231. https://doi.org/10.1016/j.jhazmat.2010.06.019

[22] Azadmanjiri J, Srivastava VK, Kumar P, Nikzad M, Wang J, Yu A (2018) Two- and three-dimensional graphene-based hybrid composites for advanced energy storage and conversion devices. J Mater Chem A 6:702–734. https://doi.org/10.1039/c7ta08748a

[23] Huang X, Qi X, Boey F, Zhang H (2012) Graphene-based composites. Chem Soc Rev 41:666–686. https://doi.org/10.1039/c1cs15078b

[24] Fang Q, Shen Y, Chen B (2015) Synthesis, decoration and properties of three-dimensional graphene-based macrostructures: a review. Chem Eng J 264:753–771. https://doi.org/10.1016/j.cej.2014.12.001

[25] Shen Y, Fang Q, Chen B (2015) Environmental applications of three-dimensional graphene-based macrostructures: adsorption, transformation, and detection. Environ Sci Technol 49:67–84. https://doi.org/10.1021/es504421y

[26] Cao X, Yin Z, Zhang H (2014) Three-dimensional graphene materials: preparation, structures and application in supercapacitors. Energy Environ Sci 7:1850–1865. https://doi.org/10.1039/c4ee00050a

[27] Cong HP, Ren XC, Wang P, Yu SH (2012) Macroscopic multifunctional graphene-based hydrogels and aerogels by a metal ion induced self-assembly process. ACS Nano 6:2693–2703. https://doi.org/10.1021/nn300082k

[28] Zhao G, Li J, Ren X, Chen C, Wang X (2011) Few-layered graphene oxide nanosheets as superior sorbents for heavy metal ion pollution management. Environ Sci Technol 45:10454–10462. https://doi.org/10.1021/es203439v

[29] Dai H, Huang Y, Huang H (2018) Eco-friendly polyvinyl alcohol/carboxymethyl cellulose hydrogels reinforced with graphene oxide and bentonite for enhanced adsorption of methylene blue. Carbohydr Polym 185:1–11. https://doi.org/10.1016/j.carbpol.2017.12.073

[30] Xu YX, Wu QO, Sun YQ, Bai H, Shi GQ (2010) Three-dimensional self-assembly of graphene oxide and DNA into multifunctional hydrogels. ACS Nano 4:7358–7362. https://doi.org/10.1021/nn1027104

[31] Chen Y, Chen L, Bai H, Li L (2013) Graphene oxide–chitosan composite hydrogels as broad-spectrum adsorbents for water purification. J Mater Chem A 1:1992–2001. https://doi.org/10.1039/c2ta00406b

[32] De Silva KKH, Huang HH, Joshi RK, Yoshimura M (2017) Chemical reduction of graphene oxide using green reductants. Carbon 119:190–199. https://doi.org/10.1016/j.carbon.2017.04.025

[33] Qiu B, Xing M, Zhang J (2018) Recent advances in three-dimensional graphene based materials for catalysis applications. Chem Soc Rev 47:2165–2216. https://doi.org/10.1039/c7cs00904f

[34] Perreault F, De Faria AF, Elimelech M (2015) Environmental applications of graphene-based nanomaterials. Chem Soc Rev 44:5861–5896. https://doi.org/10.1039/c5cs00021a

[35] Huo JB, Yu G, Wang J (2021) Adsorptive removal of Sr (II) from aqueous solution by polyvinyl alcohol/graphene oxide aerogel. Chemosphere 278:130492. https://doi.org/10.1016/j.chemosphere.2021.130492

[36] Huo J, Yu G, Wang J (2021) Efficient removal of Co (II) and Sr (II) from aqueous solution using polyvinyl alcohol/graphene oxide/MnO2 composite as a novel adsorbent. J Hazard Mater 411:125117. https://doi.org/10.1016/j.jhazmat.2021.125117

[37] Vafakhah S, Guo L, Sriramulu D, Huang S, Saeedikhani M, Yang HY (2019) Efficient sodium-ion intercalation into the freestanding prussian blue/graphene aerogel anode in a hybrid capacitive deionization system. ACS Appl Mater Interfaces 11:5989–5998. https://doi.org/10.1021/acsami.8b18746

[38] Zhang J, Yu L, Chen Y, Lu XF, Gao S, Lou XWD (2020) Designed formation of double-shelled Ni-Fe layered-double-hydroxide nanocages for efficient oxygen evolution reaction. Adv Mater 32:1906432. https://doi.org/10.1002/adma.201906432

[39] Shi S, Zhang W, Wu H et al (2020) In situ cascade derivation toward a hierarchical layered double hydroxide magnetic absorbent for high-performance protein separation. ACS Sustain Chem Eng 8:4966–4974. https://doi.org/10.1021/acssuschemeng.0c00934

[40] Wang J, Tang J, Ding B et al (2018) Self-template-directed metal-organic frameworks network and the derived honeycomb-like carbon flakes via confinement pyrolysis. Small 14:1704461. https://doi.org/10.1002/smll.201704461

[41] Wen Z, Lu J, Zhang Y et al (2020) Facile inverse micelle fabrication of magnetic ordered mesoporous iron cerium bimetal oxides with excellent performance for arsenic removal from water. J Hazard Mater 383:121172. https://doi.org/10.1016/j.jhazmat.2019.121172

[42] Hassan QU, Yang D, Zhou JP (2019) Controlled fabrication of K2Ti8O17 nanowires for highly efficient and ultrafast adsorption toward methylene blue. ACS Appl Mater Interfaces 11:45531–45545. https://doi.org/10.1021/acsami.9b12422

[43] Luo J, Fu K, Sun M et al (2019) Phase-mediated heavy metal adsorption from aqueous solutions using two-dimensional layered MoS2. ACS Appl Mater Interfaces 11:38789–38797. https://doi.org/10.1021/acsami.9b14019

[44] Goyal N, Gao P, Wang Z et al (2020) Nanostructured chitosan/molecular sieve-4A an emergent material for the synergistic adsorption of radioactive major pollutants cesium and strontium. J Hazard Mater 392:122494. https://doi.org/10.1016/j.jhazmat.2020.122494

[45] Wi H, Kim H, Oh D, Bae S, Hwang Y (2019) Surface modification of poly(vinyl alcohol) sponge by acrylic acid to immobilize Prussian blue for selective adsorption of aqueous cesium. Chemosphere 226:173–182. https://doi.org/10.1016/j.chemosphere.2019.03.101

[46] Kang S-M, Rethinasabapathy M, Hwang SK et al (2018) Microfluidic generation of Prussian blue-laden magnetic micro-adsorbents for cesium removal. Chem Eng J 341:218–226. https://doi.org/10.1016/j.cej.2018.02.025

[47] Alamudy HA, Cho K (2018) Selective adsorption of cesium from an aqueous solution by a montmorillonite-prussian blue hybrid. Chem Eng J 349:595–602. https://doi.org/10.1016/j.cej.2018.05.137

[48] Park Y, Lee Y-C, Shin WS, Choi S-J (2010) Removal of cobalt, strontium and cesium from radioactive laundry wastewater by ammonium molybdophosphate–polyacrylonitrile. Chem Eng J 162:685–695. https://doi.org/10.1016/j.cej.2010.06.026

[49] Yang H-M, Park CW, Kim I, Yoon I-H (2020) Hollow flower-like titanium ferrocyanide structure for the highly efficient removal of radioactive cesium from water. Chem Eng J 392:123713. https://doi.org/10.1016/j.cej.2019.123713

[50] Ratliff K, Mikelonis A, Duffy J (2020) Characterizing cesium sorption in freshwater settings using fluvial sediments and characteristic water chemistries. J Environ Manage 253:109688. https://doi.org/10.1016/j.jenvman.2019.109688

[51] Xing M, Zhuang S, Wang J (2020) Efficient removal of Cs(I) from aqueous solution using graphene oxide. Prog Nucl Energy 119:103167. https://doi.org/10.1016/j.pnucene.2019.103167

[52] Bostick BC, Vairavamurthy MA, Karthikeyan KG, Chorover J (2002) Cesium adsorption on clay minerals: an EXAFS spectroscopic investigation. Environ Sci Technol 36(12):2670–2676

[53] Li J, Zan Y, Zhang Z, Dou M, Wang F (2020) Prussian blue nanocubes decorated on nitrogen-doped hierarchically porous carbon network for efficient sorption of radioactive cesium. J Hazard Mater 385:121568. https://doi.org/10.1016/j.jhazmat.2019.121568